Theory of 2δ-kicked quantum rotors

C. E. Creffield,[1] S. Fishman,[2] and T. S. Monteiro[1]
[1]*Department of Physics and Astronomy, University College London, Gower Street, London WC1E 6BT, United Kingdom*
[2]*Physics Department, Technion, Haifa, IL-32000, Israel*
(Received 8 November 2005; published 2 June 2006)

We examine the quantum dynamics of cold atoms subjected to *pairs* of closely spaced δ kicks from standing waves of light and find behavior quite unlike the well-studied quantum kicked rotor (QKR). We show that the quantum phase space has a periodic, cellular structure arising from a unitary matrix with oscillating bandwidth. The corresponding eigenstates are exponentially localized, but scale with a fractional power $L\sim\hbar^{-0.75}$, in contrast to the QKR for which $L\sim\hbar^{-1}$. The effect of intercell (and intracell) transport is investigated by studying the spectral fluctuations with both periodic as well as "open" boundary conditions.

DOI: 10.1103/PhysRevE.73.066202 PACS number(s): 05.45.Mt, 32.80.Pj, 05.60.−k

I. INTRODUCTION

A recent experimental study [1] of cesium atoms subjected to *pairs* of near δ kicks using pulsed optical potentials showed behavior surprisingly different from the well-studied single-kick system, the quantum kicked rotor (QKR) or its classical counterpart, the δ-KR.

The QKR is possibly the most studied theoretical paradigm of Hamiltonian quantum chaos. It has also been well investigated experimentally, using mainly cesium atoms [2]. Its classical limit, the δ-KR, shows a gradual transition to chaotic dynamics as a function of a kick strength K (in the experiments, the kick strength is related to the intensity of the optical potential). In the large-K (chaotic) regime, typical *classical* trajectories are diffusive; to lowest order, the diffusion is a random walk in momentum, with diffusion constant $D\approx\frac{K^2}{2}$. Hence, for an ensemble of atoms, the average kinetic energy increases linearly with time, $\langle p^2\rangle\sim Dt$. Short-ranged correlations to the classical diffusion do exist, however, and their effects have also been observed experimentally [3].

In the corresponding quantum system, the QKR, while the observed behavior follows the classical dynamics for early times, the diffusion is arrested on a time scale $t^*\sim D/\hbar^2$. In experiments and calculations, an initially Gaussian momentum distribution $N(p,t=0)$ is seen for $t\gtrsim t^*$ to evolve into an exponentially localized distribution $N(p,t>t^*)\sim\exp[-|p|/L]$, where $L\sim\frac{D}{\hbar}$. This quantum suppression of chaotic diffusion is an important quantum chaos phenomenon termed dynamical localization [4]. A formal connection between dynamical localization and Anderson localization (the exponential localization of electronic wave functions in disordered metals) was made in Ref. [5].

Here we consider instead the quantum 2δ-kicked rotor (2δ-QKR): particles are subjected to *pairs* of kicks; the kicks in each pair are separated by ϵ, a small time interval while the pairs themselves are separated by a much longer time interval. The recent experimental study [1] showed that the corresponding classical diffusion involves many additional corrections from weak, but long-ranged (in time) correlations. The experiment identified periodically spaced momentum-trapping regions where the atoms absorb little energy, interspersed by regions where they absorb energy even more rapidly than the standard QKR system.

In this work we extend and develop a preliminary study of this system [6] and investigate its unexpected localization properties and spectral fluctuations. The 2δ-QKR has a novel dynamical localization regime, with localization lengths $L\propto\hbar^{-0.75}$ determined by a *fractional* exponent ($\simeq$0.75), in contrast to the well-known QKR, for which $L\propto\hbar^{-1}$. We find a similar exponent, for some parameter ranges, for the return probabilities, $P(t)=|\langle\psi(t=0)|\psi(t)\rangle|^2\sim t^{-0.75}$. We discuss the origin of the 0.75 exponents.

A key feature of interest found in [1] is that the classical momentum space is partitioned into a "cellular" structure, with momentum regions ("cells") of width $2\pi/\epsilon$ determined by the small time interval between the kicks in a pair, bounded by porous phase-space barriers. In this work, the cellular momentum structure in the classical phase space is shown to correspond to a *quantum* time-evolution operator with a periodically oscillating banded structure; the form of the bandwidth is obtained analytically here.

The corresponding eigenstates can be well localized within a single cell defined by this oscillating band; or they may extend over several cells. Here, we characterize the spectral behavior by two parameters: a filling parameter R, which quantifies the fraction of a cell that a typical state occupies, and another parameter d, which quantifies intercell transport. We consider two types of distinct (but related) delocalization transitions: (a) a $0\rightarrow1$ cell transition as eigenstates fill one cell and (b) a $1\rightarrow$ several cell transition as states delocalize from a single cell to many.

As the $0\rightarrow1$ cell transition occurs, all states extend into fractal cantori-filled regions bordering each cell; we identify a regime with spectral properties (particularly spectral variances) which, while not identical, may be compared with "critical statistics." The latter were first studied near the critical point of the Anderson metal-insulator transition (MIT) [7–12]. So-called "critical statistics" are now of much current interest in chaotic systems with classical discontinuities [non-KAM (Kolmogorov-Arnold-Moser) systems] [13–16]; they have been attributed to the effect of cantori [15,16]; however, they are not expected in KAM systems, due to their nongeneric properties. Below, we use the term critical statistics in this broader sense, rather than specifically the critical point of the MIT.

Imposing periodic boundary conditions in momentum space effectively confines the system's eigenstates to a single

cell (with toroidal geometry). Such a calculation shows a transition from Poisson to Wigner-Dyson statistics [they are of similar functional form to Gaussian orthogonal ensemble (GOE) results, so are referred to as such below, although strictly they are circular orthogonal ensemble (COE) statistics], via a new regime of intermediate statistics. We also calculate eigenstates for the open system (nonperiodic boundary conditions). This calculation yields agreement with the single-cell calculation up to the onset of delocalization, but beyond shows rather different behavior. The spectral statistics show a signature of the onset of delocalization of the eigenstates into multiple cells, characterized by a return towards Poissonian statistics.

While some of the above results were presented in a previous Letter [6], here we are able to present a full study of the spectral properties. Our main new results are the following: (1) A study of the cellular form of the unitary operator of this system. An analytical form for the bandwidth is obtained. (2) A complete numerical study of the spectral signatures of delocalization from one cell to several cells. We consider both periodic and nonperiodic boundary conditions. (3) We present an argument that the novel regime of exponential localization determined by the fractional exponent 0.75 may coincide with the dominant scaling exponent obtained in the vicinity of golden-ratio cantori. We show that an exponent ≈ 0.75 also characterizes return probabilities near the cell boundaries.

In Sec. II, we review the classical basis for the cellular structure of the 2δ-KR. In Sec. III we introduce the time-evolution operator and obtain an analytical form for its bandwidth. In Sec. IV we investigate the dynamical localization and the fractional exponent $\nu=0.75$. In Sec. V we look at the delocalization within a single cell by solving the problem "on a torus" in momentum space and compare with critical statistics. In Sec. VI we compare the behavior with a calculation with "open" boundary conditions and the signature for the onset of delocalization onto many cells. Finally in Sec. VII we give our conclusions and discussion.

II. THE 2δ-KR

We consider a system with a Hamiltonian corresponding to a sequence of closely spaced pairs of kicks:

$$H = \frac{p^2}{2} - K\cos x \sum_n [\delta(t - nT) + \delta(t - nT + \epsilon)], \quad (2.1)$$

where $\epsilon \ll T$ is a short time interval and K is the kick strength. The classical map for the 2δ-KR is then a two-kick map

$$p_{j+1} = p_j + K\sin x_j,$$

$$x_{j+1} = x_j + p_{j+1}\epsilon,$$

$$p_{j+2} = p_{j+1} + K\sin x_{j+1},$$

$$x_{j+2} = x_{j+1} + p_{j+2}\tau, \quad (2.2)$$

where τ is the time between kick pairs. It is convenient to rescale time in units of T, so that $\tau = T - \epsilon \to 1 - \epsilon$; hence, in these units, we require $\epsilon \ll 1$. Note that in the experimental realization with cold cesium atoms in [1], $0.16 \gtrsim \epsilon \gtrsim 0.04$.

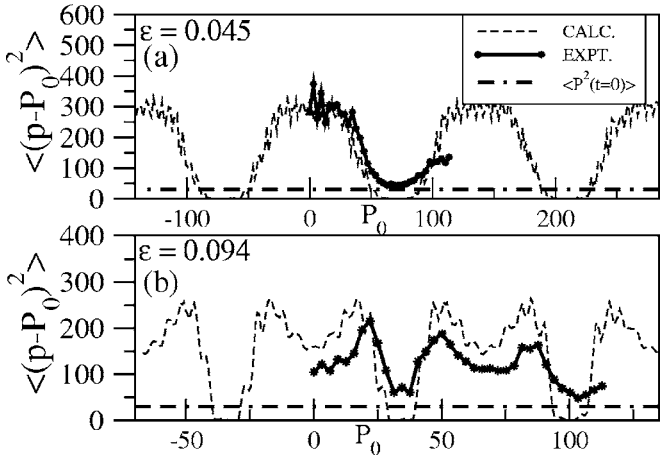

FIG. 1. Experimental results from [1] showing effects of momentum trapping. Each point indicates the energy absorbed by a cloud of cesium atoms after dynamical localization. The horizontal axis gives the initial average momenta $\langle p\rangle = P_0$ of each cloud of cesium atoms: i.e., each atomic cloud initially has a Gaussian momentum distribution well centered on P_0. The trapping regions correspond to $\langle (p - P_0)^2\rangle \simeq 0$. All the data correspond to effective values of $K=3.2$ and $\hbar = 1$.

Clearly, the limit $\epsilon = 1$ or 0 corresponds to the standard map, which describes the classical dynamics of the QKR:

$$p_{i+1} = p_i + K\sin x_i,$$

$$x_{i+1} = x_i + p_{i+1}. \quad (2.3)$$

In the experiments [1], cold atoms in a narrow momentum distribution peaked about $\langle p\rangle = p_0 \simeq (2m+1)\pi/\epsilon$ (relative to the optical lattice) were found to absorb little energy; conversely, atoms prepared near $p_0\epsilon = 2m\pi$ experience rapid energy growth up to localization. The experimental results are shown in Fig. 1. The momentum-trapping regions (where little energy is absorbed) are clearly seen. The basic mechanism of trapping is fairly intuitive: atoms for which $p_0\epsilon = (2m+1)\pi$ and $m = 0, 1, \ldots$ experience an impulse $K\sin x$ followed by another one $\simeq K\sin(x+\pi)$ which in effect cancels the first. Over time, however, there is a gradual dephasing of this classical "antiresonant" process.

In summary, the slow-diffusing, porous trapping regions provide partial barriers which partition the momentum space of this system into momentum cells of width $2\pi/\epsilon$. Since ϵ is arbitrarily small, the cells can be arbitrarily wide. Note that the limit $\epsilon \to 0$ corresponds to the cells becoming infinitely wide, so the ordinary KR behavior is recovered when the widths of typical momentum distributions are negligible compared with the cell size.

A theoretical study of the classical diffusion over longer times than a couple of kicks in [1,17] found long-ranged corrections to the uncorrelated diffusion rate, $D \simeq K^2/2$, not present in the standard map. Here and in [17] we find that the quantum and classical behaviors are both insensitive to the value of τ (the time between kick pairs) provided it is long

enough that consecutive impulses $K \sin x$ separated by a time interval τ are approximately uncorrelated. Our numerics below use $\tau \simeq 2$ or $\tau \simeq 1$. Note that while $\tau \approx 2$ is very close to the asymptotic $\tau \to \infty$ behavior, for $\tau \approx 1$ there is still some (nonqualitative though) dependence on τ. For the small time interval (within a kick pair) we use values of $\epsilon \leq 0.1$.

Below we present the corresponding quantum behavior.

III. TIME-EVOLUTION OPERATOR FOR 2δ-QKR

The time evolution operator for this system may be written

$$\hat{U}^{\epsilon} = \exp\left[-i\frac{\hat{p}^2(T-\epsilon)}{2\hbar}\right]\exp\left[i\frac{K}{\hbar}\cos x\right] \times \exp\left[-i\frac{\hat{p}^2\epsilon}{2\hbar}\right]\exp\left[i\frac{K}{\hbar}\cos x\right]. \tag{3.1}$$

In a basis of plane waves, $\hat{U}^{\epsilon}$ has matrix elements

$$U^{\epsilon}_{lm} = U^{free}_{l} U^{2-kick}_{lm} = \exp\left[-i\frac{l^2\hbar\,(T-\epsilon)}{2}\right] i^{l-m}\sum_k J_{l-k}\left(\frac{K}{\hbar}\right) \times J_{k-m}\left(\frac{K}{\hbar}\right)\exp\left[-i\frac{k^2\hbar\,\epsilon}{2}\right], \tag{3.2}$$

where the $J_n\left(\frac{K}{\hbar}\right)$ are integer Bessel functions of the first kind. It is easy to see that U^{2-kick}_{lm} is invariant if the products $K_{\epsilon} = K\epsilon$ and $\hbar_{\epsilon} = \hbar\,\epsilon$ are kept constant, while the free propagator $U^{free}_{l} = e^{-il^2\hbar(T-\epsilon)/2}$ simply contributes a near-random phase. Provided that $l^2 T\hbar \gg 2\pi$, the results are quite insensitive to the magnitude of $(T-\epsilon)\hbar$. Hence we often find it useful to consider the two scaled parameters K_{ϵ} and $\hbar_{\epsilon}$, rather than to vary K, ϵ, and $\hbar$ independently.

The result in Eq. (3.2) may be compared with the one-kick map in Eq. (2.3):

$$U^{(0)}_{lm} = \exp\left[-i\frac{l^2 T\hbar}{2}\right] J_{l-m}\left(\frac{K}{\hbar}\right). \tag{3.3}$$

The one-kick matrix for the QKR has a well-studied band structure: since $J_{l-m}(x) \simeq 0$ for $|l-m| \gg x$, we can define a bandwidth for $U^{(0)}$—namely, $b = \frac{K}{\hbar}$ (this is, strictly speaking, a *half*-bandwidth) which is independent of the angular momenta l and m. However, this is *not* the case for the matrix of U^{ϵ}.

It is shown in the Appendix that, assuming $|l-m|$ is small, we can write

$$U^{\epsilon}_{lm} \approx e^{-i\Phi} J_{l-m}\left(\frac{2K}{\hbar}\cos[l\,\hbar\,\epsilon/2]\right), \tag{3.4}$$

where the phase $\Phi = \frac{\hbar}{2}[l^2 T + \epsilon lm + \epsilon l^2] + \pi(l-m)/2$. Hence we infer a momentum dependent bandwidth, $b(p) = \frac{2K}{\hbar}\cos(p\epsilon/2)$. Figure 2 shows the calculated form of both matrices (white denotes matrix elements less than a small threshold). While $U^{(0)}$ has a constant bandwidth, the bandwidth for the matrix of U^{ϵ} oscillates with l from a maximum value $b_{max} = \frac{2K}{\hbar}$, equivalent to twice the bandwidth of $U^{(0)}$, down to a minimum value $b_{min} \sim 0$. In effect, since $b_{min} \sim 0$, U^{ϵ} is partitioned into submatrices of dimension $N = \frac{2\pi}{\epsilon\hbar}$, corresponding precisely to the momentum cells of width $\Delta p = N\hbar$ observed in the experiment.

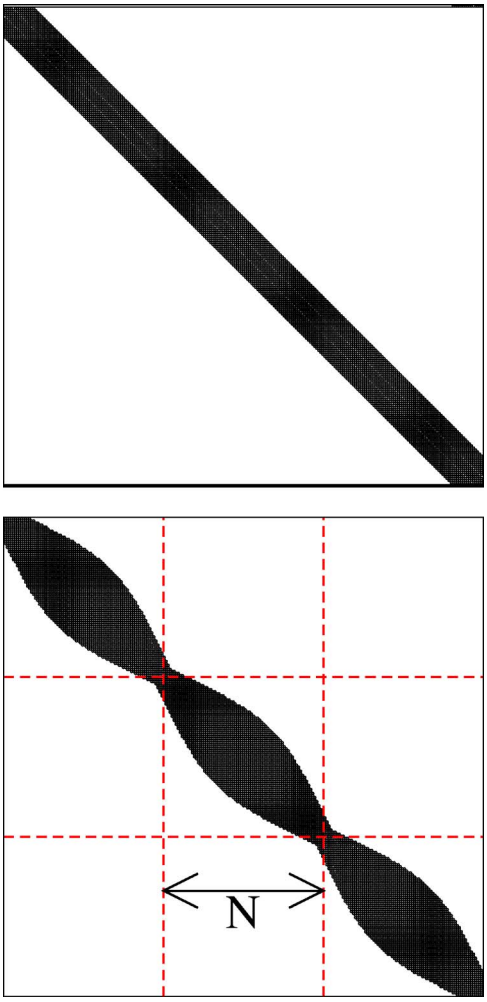

FIG. 2. (Color online) Top: Structure of time-evolution matrix for a quantum kicked rotor (QKR) in a basis of momentum states, showing the constant bandwidth structure typical of a band random matrix (BRM). Bottom: Form of U^{ϵ} for our system, the 2δ-QKR, showing the oscillating bandwidth structure. Before delocalization, eigenstates are confined within a single "momentum cell" of dimension N.

For the QKR, the localization properties of the eigenstates have been investigated extensively (see, e.g., [18] for a review). The eigenstates are exponentially localized, with momentum probability distributions $N(p) \sim \exp[-2|p|/L]$, where the localization length $L \approx \frac{K^2}{4\hbar} = b^2\hbar/4$, in the large-$K$, small-$\hbar$ limits.

For the 2δ-QKR, in the limit of small bandwidth, $\frac{2K}{\hbar} \ll N$, we define a "local" localization length for the eigenstates:

$$L(p) = b^2(p)\,\hbar/4 = \frac{K^2}{\hbar}\cos^2(p\epsilon/2). \tag{3.5}$$

This corresponds quite well with the oscillations seen in the experiment in Fig. 1(a); the energy oscillates sinusoidally from a maximum value $\langle (p-P_0)^2 \rangle \simeq 400 \sim 4L^2 \simeq 4K^4$ for $K=3.2$, $\hbar=1$ (in rescaled units) down to a minimum value $\langle (p-P_0)^2 \rangle \simeq 0$ for $P_0 \simeq \pi/\epsilon$. In contrast, Fig. 1(b) corresponds to a regime where the eigenstates are tending to fill each cell—i.e., $L(p) \to N\hbar$.

In [19,18] it was shown that the eigenstates of the QKR can also be obtained using a $U^{(0)}$ matrix of *finite* dimension N. The ratio of the localization length to N was used to characterize the degree of "filling" of the matrix $U^{(0)}$. It was shown that for a ratio $R \ll 1$ the spectral behavior is Poissonian. With increasing R, a transition to GOE behavior was observed.

For the 2δ-QKR we can also introduce a "filling factor" R defined by the ratio [19]

$$R = \frac{K^2}{N\hbar^2} = \frac{K_\epsilon^2}{2\pi\hbar_\epsilon}. \tag{3.6}$$

While for the 2δ-QKR we have a natural choice of N, determined by the position of physical boundaries (the trapping regions), the value of N in the QKR case is quite arbitrary. The problem is solved "on a torus" in momentum. The momentum periodicity of the matrix is adjusted by a choice of a rational value of the kicking period $T\hbar$ (see Sec. V below). We can then compare matrices for both $U^{(0)}$ and U^ϵ, with similar N and R.

The interesting aspect of the 2δ-QKR system is that, as we show below, we can vary the coupling between the cells independently (with some constraints on allowable parameters) from the degree of filling of each individual cell. We will show that there is a particularly interesting regime where for most eigenstates $L(p) \sim N\hbar$, but the states are still largely trapped within a single cell. We can then "open" the boundaries of the cells and investigate the delocalization regime.

In order to investigate the transport between cells, we examine the surprisingly different (relative to the QKR) process of dynamical localization in the 2δ-QKR.

IV. DYNAMICAL LOCALIZATION

A set of wave packets [all initially with $N(p, t=0) \simeq \delta(p)$] were evolved in time, using the time evolution matrix U^ϵ, for a range of K, ϵ, and $\hbar$. Figure 3 shows typical momentum distributions $N(p)$ obtained after a long time (beyond the "break time" t^* for the onset of dynamical localization). They are modulated by an exponential envelope

$$N(p) \sim \exp\left[-\frac{2(p-\bar{p})}{L_p} \right], \tag{4.1}$$

but with a regular "staircase" structure superposed. There is a steep drop in probability at each step:

$$N^+(p) = \exp[-2d] N^-(p), \tag{4.2}$$

where $N^\pm(p)$ denote the probability after and before the step, respectively. The localization length is

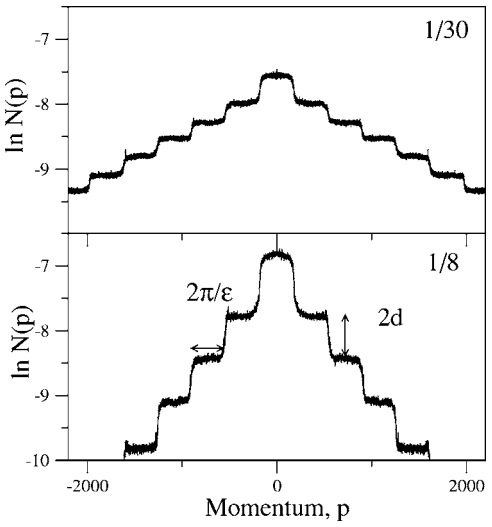

FIG. 3. Typical momentum distributions $N(p)$ found after dynamical localization for quantum wave packets of the 2δ-QKR. Here $K=20$, $\epsilon=0.0175$, and $\hbar=1/8$ and $1/30$, respectively. The $N(p)$ of the 2δ-QKR (slightly smoothed, for both eigenstates and wave packets) show a long-range tail of "staircase" form which on average follows the exponential $N(p) \sim \exp[-2(p-\bar{p})/L_p]$ where $L_p/2 = N\hbar/2d$; since $N\hbar = 2\pi/\epsilon$, the $\hbar$ dependence of L_p is determined by the drop in probability, d, at each cell boundary.

$$L_p = \frac{2\pi}{d\epsilon}. \tag{4.3}$$

The parameter d controls the transport through the cell boundaries. It also contains the $\hbar$ dependence of L_p. In Fig. 4, the dependence of d on K_ϵ and $h_\epsilon = \hbar\epsilon$ is shown. It may be seen that to very good accuracy:

$$d \propto \frac{(\hbar\epsilon)^{0.75}}{f(K_\epsilon)}, \tag{4.4}$$

where $f(K_\epsilon)$ is some function of $K\epsilon$. A rough fit yields an estimate, to within 50% or so:

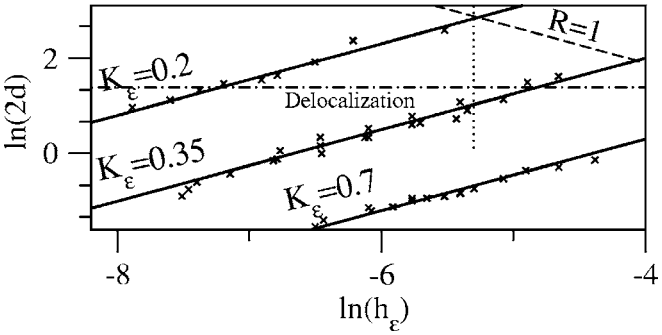

FIG. 4. Shows that $\ln(2d)$ plotted against $\ln(\hbar\epsilon)$ lies close to straight lines of invariant $K_\epsilon = K\epsilon$, with constant slope ≈ 0.75. Hence $d \propto (\hbar\epsilon)^{0.75}$ and $L_p \propto \hbar^{-0.75}$—in contrast to the well-known QKR result $L_p \propto \hbar^{-1}$. The dashed line indicates $R \simeq 1$, the one-cell filling border (i.e., $R > 1$ below the line). The *delocalization* border ($d \simeq 2$) is the dot-dashed line (i.e., $d < 2$ below the line and represents the onset of significant coupling between cells). Statistics are presented later, in Fig. 13, for points corresponding to the dotted line.

$$d \simeq \frac{3.5(\hbar\epsilon)^{0.75}}{K_\epsilon^3}. \tag{4.5}$$

Hence we obtain the surprising result that for the 2δ-QKR, the localization length has an $\hbar$ dependence with a *fractional* power, $L_p \sim \hbar^{-0.75}$. In comparison, for the QKR, $L_p \sim \hbar^{-1}$.

It is interesting to consider the origin of the $\hbar^{-0.75}$ behavior. In fact, the first few steps of the staircase can be seen in experiments with optical lattices of [1]. An earlier experiment [21] with pairs of broad pulses (as opposed to pulses short enough in duration to approximate δ kicks) also showed a steep drop in probability over a narrow momentum region. This was identified as due to the presence of cantori. The finite pulse system does not have the momentum periodicity (and hence the generic character) of the 2δ-kicked system and is effectively integrable at large p. Nevertheless, the classical dynamics is similar to the 2δ-QKR for $p \sim 0$. The QKR shows analogous behavior: for pulses of finite duration, the classical dynamics is similar to the δ-kicked system for p small.

We can examine the classical behavior in the trapping regions. Starting from the two-kick map, Eq. (2.2), and expanding our initial momenta around the trapping momenta $p_j \simeq P_n + \delta p^j$ where $P_n = (2n+1)\pi/\epsilon$, we can write

$$p_{j+2} = p_j + K \sin x_j + K \sin[x_j + (2n+1)\pi + \delta p^j \epsilon + K\epsilon \sin x_j]. \tag{4.6}$$

We can expand the trigonometric expressions, making small-angle approximations, if we assume $\delta p^j \epsilon \ll 2\pi$ and $K\epsilon \ll 2\pi$. In the trapping regions we then obtain an approximate one-kick map

$$p_{j+2} \simeq p_j - K^2 \frac{\epsilon}{2} \sin 2x_j - K\delta p^j \epsilon \cos x_j,$$

$$x_{j+2} \simeq x_j + p_{j+2} T. \tag{4.7}$$

The small-angle assumption $\delta p^j \epsilon \ll \pi$ constrains Δp, the effective width of the trapping region,

$$\Delta p \sim 1/\epsilon. \tag{4.8}$$

A study of the Poincaré surfaces of section (SOS) may be found in Ref. [17]. To summarize, at the center of the trapping region, where $\delta p^j = 0$, only the $\sin 2x$ kick in Eq. (4.7) is significant, so the classical SOS show structure very similar to a "period-doubled" standard map with impulse $V'(x) = K_{\text{eff}} \sin 2x$ where K_{eff} is an effective kick strength, $K_{\text{eff}} \simeq K^2 \frac{\epsilon}{2}$. However, farther out within the trapping region, the SOS show that it is the $\cos x$ kick in Eq. (4.7) which is dominant and the island structure is similar to that of a standard map with impulse

$$V'(x) \simeq K\delta p \epsilon \cos x. \tag{4.9}$$

Given the importance of the $K\epsilon$ scaling seen in Fig. 4 (rather than a $K^2\epsilon$ scaling) we suggest that the $K_{\text{eff}} \cos x$ form of Eq. (4.7) determines the quantum behavior. This implies that regions with

$$K\delta p^j \epsilon \gg K^2 \frac{\epsilon}{2} \tag{4.10}$$

dominate transport. This will be the case if δp_j is large; from Eq. (4.8), we deduce that this implies the criterion $K\epsilon \ll 1$. However, if $K\epsilon$ is too small, the phase space will be too regular. Hence, values of $K\epsilon \approx 0.1-0.3$ seem indicated.

In any case, the resonance structure in much of the trapping regions is always locally similar to the standard map, but with a varying effective kick strength (and phase of the impulse). For the standard map the last invariant phase-space manifolds correspond to $p/(2\pi) \simeq \phi$ or $\simeq 1-\phi$ where ϕ is the golden ratio. The fractal remnant of this last manifold plays a role in transport in the standard map for $K \simeq 1-3$. Here, this would suggest $\delta p K\epsilon \approx 1-3$ and $\delta p \sim 10$ [22].

The scaling properties of the phase space around the golden-ratio cantori were investigated in Ref. [23]. A characteristic exponent $\sigma_s \approx 0.75$ was found in directions dominated by elliptic fixed points. We term this the stable or dominant exponent. On the other hand, $\sigma_u \approx 0.66$ was found in directions dominated by hyperbolic fixed points. We term this the unstable or subdominant exponent.

Previous studies of the QKR [24] found a $L \propto \hbar^{+\sigma}$ scaling, with $\sigma \simeq \sigma_u \simeq 0.66$, for momenta near the range $1-\phi < pT/(2\pi) < \phi$. In [25], a $L \propto \hbar^{+\sigma_u}$ scaling was associated with a tunneling-type process (termed "retunneling"). An abrupt change to a regime with $L \propto \hbar^{-\sigma}$, with $\sigma \approx 0.5$, was also observed and was attributed to a localization process which dominates when transport through the fractal cantoral regions is more "open." In that work, it was argued that the process has similarities with dynamical localization.

The 2δ-QKR results, with a negative sign on the exponent $L \sim \hbar^{-0.75}$, correspond to a localization regime and are consistent with quantum probability "sticking" mostly to directions where there are (or were, at lower K) elliptic fixed points. One might speculate why no previous studies uncovered a regime dominated by σ_s; we note that in [24,25] the $L \sim \hbar^{+0.66}$ scaling refers to a local region. These are regimes where there are many stable islands and overall diffusion in each phase-space manifold is either absent or rather slow. Here, in contrast, part of phase space is taken by very chaotic, fast-diffusing regions, with trajectories which roam freely over large areas of phase space; the only appreciable localization occurs at the stabler parts of Cantoral remnants.

We also calculated return probabilities $P(t)$ of the quantum wave packets with time, averaged over 100 initial starting conditions close to the center of the trapping region,

$$P(t) = (1/100) \sum_{l_1}^{l_2} \langle P_l(t) \rangle, \tag{4.11}$$

where $P_l(t) = |\langle \psi(t) | \psi_l(t=0) \rangle|^2$. The initial condition was taken to be an angular momentum eigenstate $\psi_l(t=0) = |l\rangle$. The results were averaged from $l_1 = \pi/\epsilon\hbar$ to $l_2 = l_1 + 100$. Figure 5 shows plots of $P(t)$, which show that $P(t)$ decays as $t^{-0.75}$ up to the break time. For the lowest values of $K\epsilon$, the $t^{-0.75}$ decay is not apparent since the wave packet localizes almost immediately.

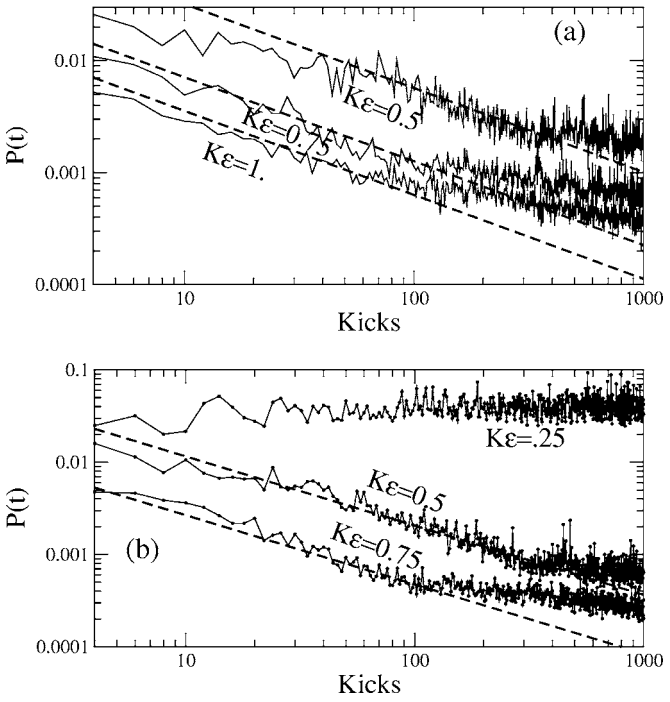

FIG. 5. Return probabilities for wave packets prepared near the center of the trapping regions indicating a $P(t) \sim t^{-0.75}$ decay, before localization. The dashed straight lines indicate a slope of −0.75. Note that at the lowest value of $K\epsilon = 0.25$, wave packets prepared at the center of the trapping region do not spread in momentum. (a) $\hbar = 1/8$ and (b) $\hbar = 1/16$.

A well-known relation between power-law return probabilities and the spectral statistics (variances) has been investigated for "critical statistics" in non-KAM billiards or the Anderson transition [8,10,12,16]. While the present systems has important differences (it is a smooth KAM system; it has a cellular structure and an oscillating band unitary matrix), the preeminence of the single fractional exponent motivates an investigation of the spectral properties. A mixed phase-space regime (with a mixture of a chaotic regions and stable islands) can indeed exhibit fractional return probabilities [26], but it will typically have many competing exponents, characterizing only local regions of phase space. The quantum localization properties are thus not generic and depend sensitively on the detailed phase-space structure. To our knowledge, there is no similar study of a KAM system so globally characterized by a single fractional exponent.

We investigate the statistics as a function of the filling factor R and the intercell transport parameter d. Calculations were done for two types of boundary conditions: periodic boundary conditions and "open" (nonperiodic) boundary conditions. These are discussed in turn below.

V. EIGENSTATES: PERIODIC BOUNDARY CONDITIONS

We may keep the dimension of the unitary matrix U to a finite value N by making the momentum periodic with period $N\hbar$, following the approach in [19,20,18]. In order to preserve unitarity we must use a resonant value of $\hbar\epsilon$. We take

$$\hbar\epsilon = \frac{2\pi}{N} \tag{5.1}$$

and then

$$\hbar\tau = \hbar\,(T-\epsilon) = M\hbar\,\epsilon, \tag{5.2}$$

where M is the closest integer to $(T-\epsilon)/\epsilon$. We then construct a unitary matrix with elements:

$$U_{ln}(\tau_j) = \frac{1}{N}\exp\left[-i\tau_j(l+\theta_x)^2/2\right] \times \sum_{k=-N_1}^{N_1} \exp\left[i\frac{K}{\hbar}\cos\frac{2\pi}{N}(k+\theta_p)\right] \times \exp\left[\frac{2\pi i}{N}(k+\theta_p)(l-n)\right]. \tag{5.3}$$

We may have $\tau_1 = \hbar\epsilon$ or $\tau_2 = m\tau_1$. Here $N_1 = (N-1)/2$. We construct the full two-kick matrix of dimension N:

$$U_\epsilon(N) = U(\tau_1)U(\tau_2), \tag{5.4}$$

which is then diagonalized to obtain N eigenvalues and eigenstates. We may compare the results with the QKR equivalent

$$U^0(N) = U(T\hbar). \tag{5.5}$$

Here $\hbar = 2M\pi/N$, where M is an integer (noncommensurate with N) which determines the momentum width of the matrix—i.e., $N\hbar = 2M\pi$. Unlike the 2δ-QKR, there is no underlying physical cellular phase-space structure to justify the choice of a particular M, N.

Note the dependence of the matrix elements on two Bloch phases: θ_p is a Bloch phase in the p direction while θ_x, the Bloch phase in the x direction, is the quasimomentum. If $\theta_p \neq 0, \pi$, parity is not a good quantum number and we may use all eigenvalues in the statistics, regardless of parity. It is customary (e.g., [26,16]) to calculate spectra for several θ_p to improve significance. In practice, we found that for the 2δ-QKR, even for sizable K, there are very localized states which are too removed from the boundaries and generate pairs of parity-related pairs of near degeneracies. The parity conservation effects is more effectively eliminated by, in addition to $\theta_p \neq 0, \pi$, also having $\theta_x \neq 0, 0.5$. The cantori effects we investigate are not affected by a nonzero quasimomentum, and thus we average over several quasimomenta.

Effects of cantori in 0→1 cell transition: QKR versus 2δ-QKR

We have calculated eigenvalues of the unitary matrix for a range of values of M, N, and K. Below we compare nearest-neighbor $[P(S)]$ distributions and spectral variances $\Sigma_2(L) = \langle L^2\rangle - \langle L\rangle^2$, of the 2δ-QKR with those of the QKR as a function of the filling factor $R = K^2/N\hbar^2$. We present results for $M = 25$ (i.e., $\epsilon = 0.04$) and values *close* to $N = 625, 1250$, and 2500 (one cannot have N, M commensurate).

In Fig. 6 we show typical nearest-neighbor spacings (NNS) distributions for $R \ll 1$, $R \sim 1$, and $R \gg 1$. For both

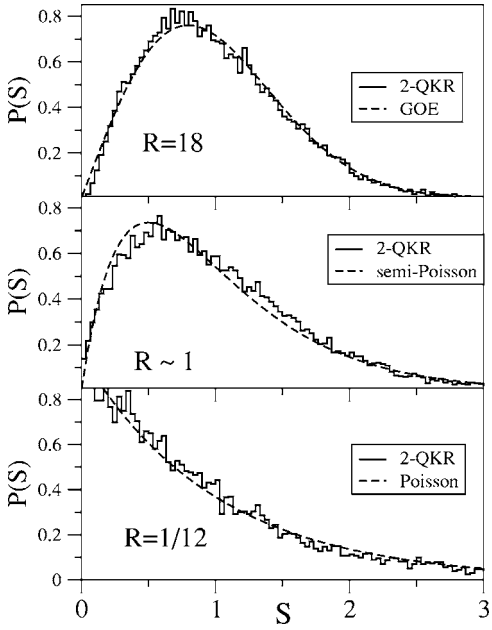

FIG. 6. Typical nearest-neighbor distributions $P(s)$, for periodic boundary conditions, for the 2δ-QKR as a function of the filling factor R. The distributions are Poissonian for small R, intermediate for $R\sim 1$, and GOE for sufficiently large R. Although the intermediate case never exactly follows the semi-Poisson distribution $[P(s)=4se^{-2s}]$, a comparison is useful, so is shown in the middle figure.

single- and double-kicked systems, the behavior evolves from Poissonian to GOE, via an intermediate distribution at $R\sim 1$. While the 2δ-QKR does not exactly show the intermediate semi-Poisson form, it can get quite close, and so a comparison is helpful. Here we quantify the deviation of $P(S)$ from $P_P(S)$ and $P_{GOE}(S)$, its Poisson and GOE limits, respectively, with a quantity Q[27]:

$$1-Q=\frac{\int_0^{S_0}[P(S')-P_{GOE}(S')]dS'}{\int_0^{S_0}[P_P(S')-P_{GOE}(S')]dS'}. \qquad (5.6)$$

Hence $Q=0$ indicates a Poisson distribution, while $Q=1$ signals a GOE distribution. We take $S_0=0.3$. In Fig. 7 we plot Q as a function of R. We find that while the QKR moves rapidly from Poisson to GOE for $R\sim 1$, the 2δ-QKR curve abruptly changes slope and the distribution evolves much more slowly towards the GOE. We identify this as the regime where delocalization of the eigenstates over the whole cell is constrained by the cantori regions bordering the cells. A fit to alternative functions such as the Berry-Robnik function[28] gives a qualitatively similar picture.

In Fig. 8 we show that the variances are close to Poissonian $\Sigma_2(L)\simeq L$ for small R and are close to the GOE for large R. However, for $R\sim 1$ there is a regime with nearly linear slope, $\Sigma_2(L)\simeq \chi L$, for $1\ll L\ll N$. We fitted the slopes of the $\Sigma_2(L)$ to the best straight line in the range $L=7\rightarrow 37$. We note that the graphs are not necessarily very linear every-

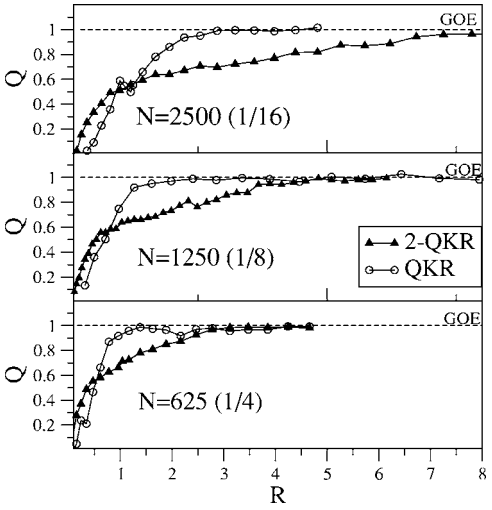

FIG. 7. Comparison of the transition from Poissonian ($Q=0$) to GOE ($Q=1$) NNS statistics for the QKR relative to the 2δ-QKR, as a function of the filling factor $R=K^2/N\hbar^2$. While the QKR makes a rapid transition from Poisson to GOE for $R\simeq 1$, the 2δ-QKR, on the other hand, shows a clear change in slope where delocalization of the quantum eigenstates is hindered by the fractal cell borders. Here $M=25$; the values shown in brackets are approximate values of $\hbar=2\pi M/N$; to avoid commensurability of M and N, actual values of N used were 2513, 1259, and 629.

where: in certain regimes there is a pronounced curvature. Nevertheless, the procedure does give an indication of the average slope. While the $N=2500$ results may remain linear out to $L\approx 100$, the $N=625$ results saturate at much lower L; hence, the $L=7-37$ range is a compromise, good for all three cell sizes.

In Fig. 9 we plot the slopes χ (the level compressibilities) for the 2δ-KR. We see that above $R\simeq 1$ there is, relative to the QKR, a plateau in the level compressibility, where $\chi\approx 0.125$. This behavior is completely absent in the QKR: for $R\simeq 1$, the values of χ evolve rapidly towards the GOE limit.

We recall the results [8] for the level compressibilities of the Anderson MIT. It is predicted that asymptotically the variances have a linear form, for $L\gg 1$:

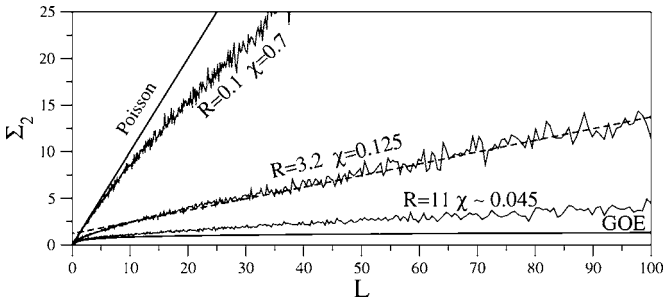

FIG. 8. Typical number variances $\Sigma_2(L)$ as a function of R for the 2δ-QKR. We use the best fit to the slope to estimate the level compressibility χ. For R small, we have Poissonian statistics and $\Sigma_2(L)\simeq \chi L\simeq L$. For sufficiently large L, $\Sigma_2(L)\sim \ln(L)$ is far from linear; in this case, the value $\chi<0.05$ is simply an indication that $\Sigma_2(L)$ is close to the GOE limit. We identify an intermediate regime where $\Sigma_2(L)\sim \chi L$ for $1\ll L\ll N$ (here $N=2513$) with $\chi\sim 0.13$, corresponding to a similar range of R as the regime seen in Fig. 7.

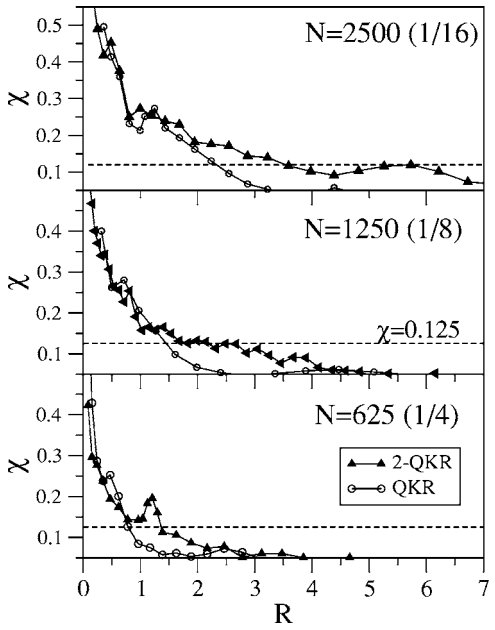

FIG. 9. The slopes (χ) of the variances $\Sigma_2(L)$ as a function of the filling factor $R=K^2/N\hbar^2$. This figure compares the transition from Poissonian ($\chi=1$) to GOE ($\chi<0.05$) for the QKR with that of the 2δ-QKR. Parameters are similar to Fig. 7. The QKR makes a rapid transition to GOE at $R\simeq 1$ (with the exception of the small minimum seen at $R\simeq 1$ and $N=2500$ which corresponds to a classical antiresonance $K\simeq\pi$). The 2δ-QKR, on the other hand, shows an approximate plateau near $\chi\simeq 0.125$, the value that would be expected from the "critical" statistics relation $\chi\simeq 1/2(1-D_2)$ if $D_2\simeq 0.75$.

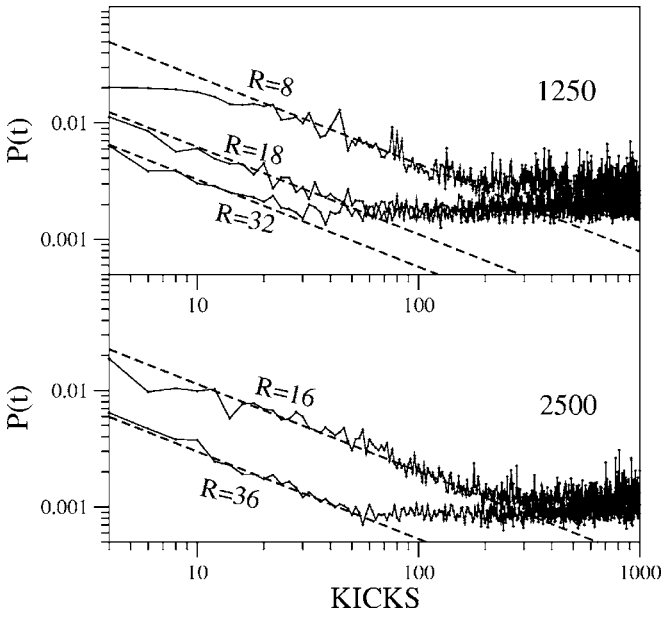

FIG. 10. Return probabilities for the finite-dimensional problem, for similar parameters to Fig. 5. The $P(t)$ still decay as $t^{-0.75}$ for $t<t^*$; but $P(t)\to 2/N$ for $t\to\infty$.

$$\Sigma_2(L)\approx\chi L, \tag{5.7}$$

where

$$\chi\approx(1-D_2/D)/2<1 \tag{5.8}$$

and D is the spatial dimension. D_2 is a multifractal exponent related to the inverse participation ratio. This behavior corresponds [8], in the MIT, to return probabilities which decay as $P(t)\sim t^{-D_2}$ and is considered a "fingerprint" of critical systems, even in systems without disorder such as the non-KAM billiards [16].

Here we calculate the return probabilities using the eigenstates $|\alpha\rangle$ and eigenvalues $e^{i\omega_\alpha}$ of the N-dimensional matrix. We calculate

$$P_l(t)=\sum_\alpha |e^{i\omega_\alpha}|\langle l|\alpha\rangle|^2|^2 \tag{5.9}$$

and average $P_l(t)$ over different starting conditions in the trapping regions $|l\rangle$, exactly as in Eq. (4.11).

We note that in Eq. (4.11), the $P(t)$ are obtained independently of the eigenstates by direct time evolution of a wave packet in the *unbounded* system. The behavior in Fig. 10 is very similar to that in Fig. 5, and again a decay rate $P(t)\sim t^{-0.75}$ is apparent. However, $P(t)$ in Fig. 10 saturates to a larger value than for Fig. 5, where the wave packets are not restricted to a finite cell. For the finite-N case $P(t)\to 2/N$ as $t\to\infty$ (the factor of 2 is attributed to weak localization [29]).

We also observe that for $R\simeq 1$, in the regime with $\chi\sim 0.125$, wave packets started in the trapping regions localize too rapidly to demonstrate the power-law decay.

We see here that $\chi\approx 0.125=(1-\nu)/2$ would imply $\nu\approx 0.75$, close to the exponent we obtained previously. It is tempting to suggest that here ν, the dominant exponent near the golden-ratio cantori, may play a role equivalent to the multifractal exponent D_2 in the Anderson MIT. Nonetheless, it should be noted that this purely numerical observation is not conclusive.

Unlike the billiard systems, here phase space is not homogeneously filled with cantori. However, underlying classical trajectories may spend considerable time trapped within the fractal trapping regions which border the cell. The corresponding typical quantum states for $R>1$ also sample the cantori region, but localize inhomogeneously in the fractal regions. As R increases, however, the distribution delocalizes into a more typically ergodic regime and the variances evolve towards the GOE ($\Sigma_2(L)\sim\ln L$) limit.

VI. OPEN BOUNDARY CONDITIONS: DELOCALIZATION FROM SINGLE TO MULTIPLE CELLS

We diagonalize the matrix of U^ϵ, with elements given by Eq. (3.2), in a basis of a given parity and dimension $N_{tot}=10\,000\gg N$, for various K, ϵ, and $\hbar$, and obtain all eigenvalues and eigenvectors. For our calculations the cell dimensions are in the range $N\simeq 600-2500$ and hence each diagonalization spans N_{tot}/N cells (fewer are kept since states in the cells at the edges of the matrix are discarded).

For instance, results presented below have $\epsilon=0.04$ and $\hbar=1/8$. Hence each cell contains $N=2\pi/(\hbar\epsilon)\simeq 1257$ states, and so each diagonalization yields up to seven complete cells. Each full spectrum of length $N_{tot}=10\,000$ is now split

into eight single-cell subspectra. We assign the ith eigenvalue to the mth cell if

$$(2m-1)\frac{\pi}{\epsilon} \leq \overline{p_i} < (2m+1)\frac{\pi}{\epsilon}. \tag{6.1}$$

We calculate $P(S)$ and variances separately for each of these subspectra of length $N=1257$. We then average the statistical distributions of 10–40 cells to obtain smoother distributions. We diagonalize U^{ϵ} for basis states between $l=10\,000$ and 20 000 as easily as states between 70 000 and 80 000, for example, so as large a number of sets of seven subspectra may be obtained as required. For the most delocalized spectra (with $K=14$) only a single central cell of about 1250 states was sufficiently well converged to be used for statistics.

Figure 11 investigates how much of the momentum probability for each eigenstate is contained in the cell it was assigned to: for $R \leq 1$ and $d>2$ the eigenstates are essentially fully contained within the cells they are assigned to. However, at the onset of delocalization, this procedure begins to fail; the expectation value $\overline{p_i}$ of an eigenstate may assign it to the mth cell; however, most of its probability may in fact be trapped in neighboring cells. This means that increasingly, the eigenvalues of the subspectra become uncorrelated and we can expect to see a return towards Poissonian statistics.

The apparent "failure" of this procedure, in fact, provides a good marker of delocalization from one to several cells. In

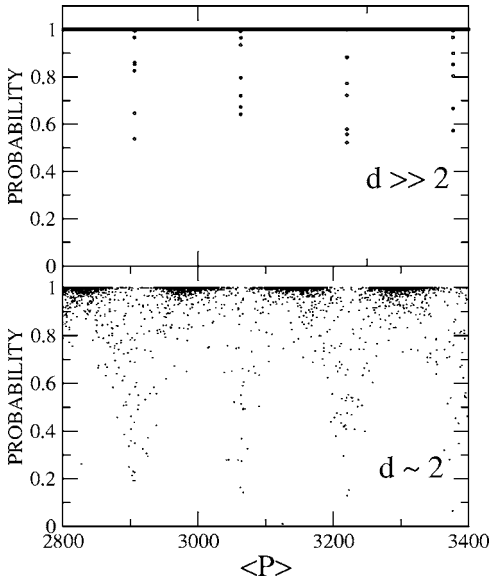

FIG. 11. The effect of delocalization onto multiple cells: each point indicates the total probability of finding a given eigenstate in the cell which contains its average momentum $\langle p \rangle$. Well below the delocalization border ($d \gg 2$), all states are fully contained in their assigned cell (barring a few edge states at the boundary of each cell). But at the "delocalization border" ($d \simeq 2$), a proportion of states have appreciable probability in neighboring cells—in fact, about 2% of states have less than half of their probability in their assigned cell. Results correspond to $\epsilon=0.04$, $\hbar=1/8$, and $K=3$ (upper figure) or $K=7$ (lower figure).

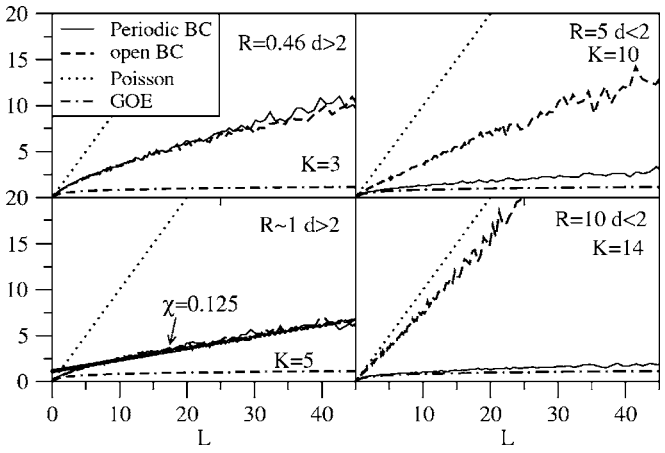

FIG. 12. The effects of delocalization onto multiple cells on the spectral variances. Variances obtained with periodic boundary conditions ($N \approx 1250$) are compared with "open" boundary conditions (BC's) ($N_{tot}=10\,000$, $N \approx 1250$, $M=51$). For $d>2$, the eigenstates are well confined within a single cell and there is no significant difference between "open" and "closed" BC's. When $d<2$, the results are sensitive to the BC's. While the "closed" (periodic) BC's results tend to the GOE, the "open" results revert towards Poissonian statistics.

contrast, the periodic boundary conditions presented in the previous section could indicate only the degree of "filling" of each single cell. Finally, we compare the spectral fluctuations for the two different types of boundary conditions (periodic versus open) in Figs. 12–14. In Figs. 12 and 13 we show that the spectral variances are insensitive to the boundary conditions for $d>2$. However, for $d<2$ the variances with periodic boundary conditions gradually make a transition to GOE behavior, while the variances for the "open" system begin to return back to Poissonian statistics. Figure 14 shows that the NNS distributions closely follow the same trends.

VII. CONCLUSIONS AND DISCUSSION

In conclusion, we have investigated the quantum behavior of atoms exposed to pairs of δ kicks and shown that the cellular structure arises from a novel oscillatory band structure of the corresponding unitary matrix. One consequence is a new type of localization-delocalization transition not seen in the QKR, where states delocalize from a single cell to many, associated with a characteristic spectral signature (the return to Poissonian statistics).

We have also found certain scalings $L \sim \hbar^{-0.75}$ and $P(t) \sim t^{-0.75}$ which we argue result from the bands of cantori present on the borders of each cell. We argue also that the 0.75 exponent may be identified with the dominant stability exponent obtained previously near golden-ratio cantori. We show that the spectral fluctuations (both the NNS and spectral variances) show important differences with the QKR in regimes where the delocalization of eigenstates is hindered by cantori.

By implication, the study shows that the behavior of cold atoms in double-pulsed standing waves of light is quite different from the single-pulsed systems. Some aspects were

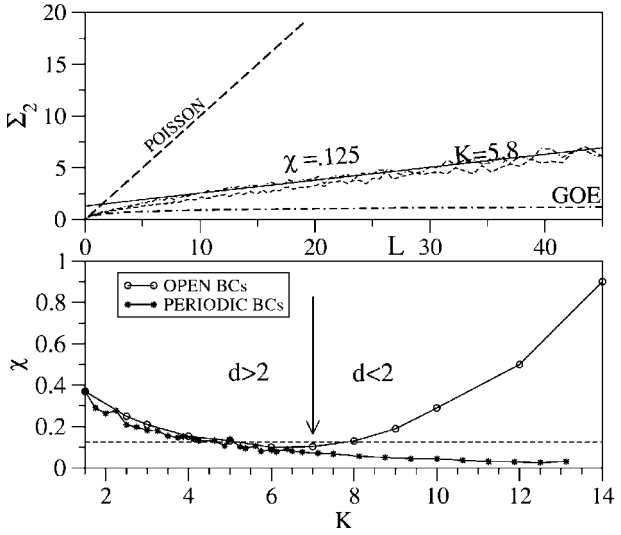

FIG. 13. Upper figure: the variances (Σ_2 statistics) for open BC's can pass close to the so-called "critical" regime of near-linear variances, with a slope close to $\chi \approx 0.125$. Lower figure: comparison of values of χ for "open" BC's (a unitary matrix of dimension $N_{tot}=10\,000$ is diagonalized to obtain cells of dimension $N \approx 1250$) with "closed" BC's (a finite matrix of dimension $N \approx 1250$, $M=51$ is diagonalized, with periodic BC's to retain unitarity). The results are in excellent agreement before delocalization $d>2$. After delocalization $d<2$, the "closed" BC's tend to GOE, the "open" BC's tend to Poissonian behavior, providing a clear signature of delocalization into multiple cells.

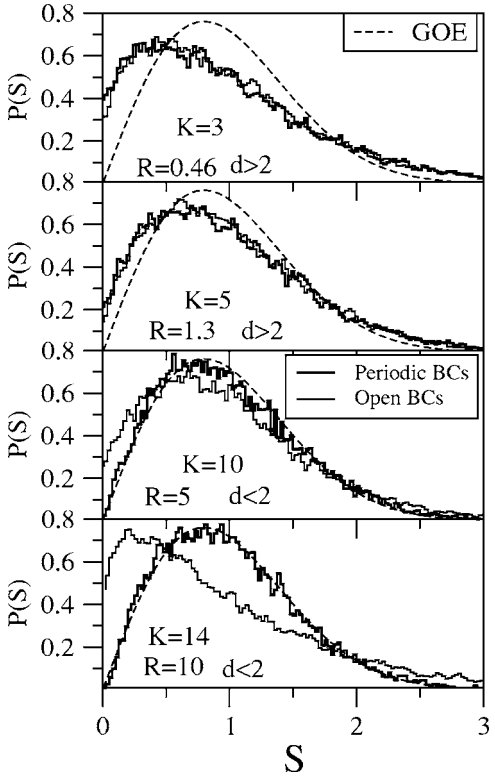

FIG. 14. Behavior of NNS distributions equivalent to the results in Figs. 12 and 13. The results are insensitive to BC's before the onset of delocalization onto multiple cells $d>2$. After delocalization $d<2$, the "closed" BC's yield the GOE and the "open" BC's tend to more Poissonian behavior.

already identified in the experiments of [1] and may have applications in atom optics and atom chips, possibly as a mechanism for selecting atoms according to their momentum.

ACKNOWLEDGMENTS

We are grateful to Phil Jones for the use of the experimental data in Fig. 1. C.E.C. and T.S.M. acknowledge support from the Engineering and Physical Sciences Research Council. We acknowledge the hospitality of the organizers of the workshop on "Resonances and Periodic Orbits: Spectrum and Zeta Functions in Quantum and Classical Chaos" at Institut Henri Poincaré, Paris, in 2005. S.F. would like to thank Richard Prange and Edward Ott for the hospitality at the University of Maryland, where the work was completed.

APPENDIX: DERIVATION OF THE APPROXIMATION [Eq. (3.4)] FOR U^{ϵ}_{lm}

In this appendix Eq. (3.4) will be derived for small ϵ. The crucial point in this derivation is that contributions to the sum in Eq. (3.2) of terms where

$$|k-l| \gg K/\hbar\,, \quad |k-m| \gg K/\hbar \tag{A1}$$

are negligible. This implies that for terms that contribute appreciably, k is close to l and m. Therefore the corresponding operator $\hat{k}=\hat{p}/\hbar$ can be written in the form

$$\hat{k} = k_0 + \hat{k}_1, \tag{A2}$$

where k_0 is a number close to l and m. Appreciable contributions to the sum are found only for

$$|k_1| \leq K/\hbar\,. \tag{A3}$$

If $\hbar\epsilon(K/\hbar)^2 \ll 1$, as is the case for small ϵ, the condition $\hbar\epsilon k_1^2 \ll 1$ is satisfied, justifying the approximation

$$\exp\left[-i\frac{\hat{p}^2\epsilon}{2\hbar}\right] = \exp\left[-i\frac{\hbar\epsilon\hat{k}^2}{2}\right] \approx \exp\left[-i\frac{\hbar\epsilon k_0^2}{2}\right]\exp\left[-i\hbar\,\epsilon k_0\hat{k}_1\right]. \tag{A4}$$

Substitution in Eq. (3.1) with $\hat{k}_1=-i\partial/\partial x$ and making use of the fact that $\exp\left[-i\hbar\epsilon k_0\frac{\partial}{\partial x}\right]$ is the shift operator, one finds

$$U^{\epsilon}_{lm} \approx e^{-i(\hbar/2)[(T-\epsilon)l^2+\epsilon k_0^2]}\langle l|e^{-i(K/\hbar)[\cos x+\cos(x-\hbar\epsilon k_0)]}e^{-i\hbar\epsilon k_0\hat{k}_1}|m\rangle, \tag{A5}$$

which reduces to

$$U^{\epsilon}_{lm} \approx e^{-i(\hbar/2)[(T-\epsilon)l^2+\epsilon k_0^2+2\epsilon k_0 m]} \times \langle l|e^{-i(2K/\hbar)[\cos(x-\hbar\epsilon k_0/2)\cos(\hbar\epsilon k_0/2)]}|m\rangle. \quad \text{(A6)}$$

The matrix element is calculated with the help of the identity

$$\frac{1}{2\pi}\int_{-\pi}^{\pi} dx e^{-i\beta\cos(x-\alpha)}e^{imx} = e^{im(\alpha-\pi/2)}J_m(\beta), \quad \text{(A7)}$$

resulting in

$$U^{\epsilon}_{lm} \approx e^{-i(\hbar/2)[(T-\epsilon)l^2+\epsilon k_0^2+\epsilon k_0 m+\epsilon k_0 l]}e^{i(\pi/2)(l-m)} \times J_{m-l}\left[\frac{2K}{\hbar}\cos\left(\frac{1}{2}\hbar\,\epsilon k_0\right)\right]. \quad \text{(A8)}$$

Indeed appreciable contributions are found only for $|m-l| \lesssim 2K/\hbar$, in agreement with (A1). Since k_0 is close to l and m, within the approximation of this appendix , it can be replaced by one of these. The substitution $k_0=l$ results in Eq. (3.4).

[1] P. H. Jones, M. M. Stocklin, G. Hur, and T. S. Monteiro, Phys. Rev. Lett. **93**, 223002 (2004).

[2] F. L. Moore, J. C. Robinson, C. F. Bharucha, B. Sundaram, and M. G. Raizen, Phys. Rev. Lett. **75**, 4598 (1995); H. Ammann, R. Gray, I. Shvarchuck, and N. Christensen, *ibid.* **80**, 4111 (1998); P. Szriftgiser, J. Ringot, D. Delande, and J. C. Garreau, *ibid.* **89**, 224101 (2002); M. B. d'Arcy, R. M. Godun, M. K. Oberthaler, G. S. Summy, K. Burnett, and S. A. Gardiner, Phys. Rev. E **64**, 056233 (2001); S. Schlunk, M. B. d'Arcy, S. A. Gardiner, and G. S. Summy, Phys. Rev. Lett. **90**, 124102 (2003); G. Hur, C. E. Creffield, P. H. Jones, and R. S. Monteiro, Phys. Rev. A **72**, 013403 (2005).

[3] B. G. Klappauf, W. H. Oskay, D. A. Steck, and M. G. Raizen, Phys. Rev. Lett. **81**, 4044 (1998).

[4] G. Casati, B. V. Chirikov, F. M. Izraelev, and J. Ford, in *Lecture Notes in Physics*, Vol. 93 (Springer, Berlin, 1979), p. 334.

[5] S. Fishman, D. R. Grempel, and R. E. Prange, Phys. Rev. Lett. **49**, 509 (1982).

[6] C. E. Creffield, G. Hur, and T. S. Monteiro, Phys. Rev. Lett. **96**, 024103 (2006).

[7] B. I. Shklovskii, B. Shapiro, B. R. Sears, P. Lambrianides, and H. B. Shore, Phys. Rev. B **47**, 11487 (1993).

[8] J. T. Chalker, I. V. Lerner, and R. A. Smith, Phys. Rev. Lett. **77**, 554 (1996).

[9] B. Huckestein and L. Schweitzer, Phys. Rev. Lett. **72**, 713 (1994).

[10] V. E. Kravtsov and K. A. Muttalib, Phys. Rev. Lett. **79**, 1913 (1997).

[11] D. Braun, G. Montambaux, and M. Pascaud, Phys. Rev. Lett. **81**, 1062 (1998).

[12] F. Evers and A. D. Mirlin, Phys. Rev. Lett. **84**, 3690 (2000); A. D. Mirlin, Phys. Rep. **326**, 259 (1999).

[13] E. B. Bogomolny, U. Gerland, and C. Schmit, Phys. Rev. E **59**, R1315 (1999).

[14] J. Wiersig, Phys. Rev. E **65**, 046217 (2002).

[15] A. M. Garcia-Garcia and J. J. M. Verbaarschot, Phys. Rev. E **67**, 046104 (2003).

[16] A. M. Garcia-Garcia and J. Wang, Phys. Rev. Lett. **94**, 244102 (2005).

[17] M. Stocklin and T. S. Monteiro, e-print physics/0408088.

[18] F. M. Izraelev, Phys. Rep. **196**, 299 (1990).

[19] M. Feingold, S. Fishman, D. R. Grempel, and R. E. Prange, Phys. Rev. B **31**, 6852 (1985); M. Feingold and S. Fishman, Physica D **25**, 181 (1987); M. Feingold, S. Fishman, D. R. Grempel, and R. E. Prange, Phys. Rev. Lett. **61**, 377 (1988).

[20] S.-J. Chang and K.-J. Shi, Phys. Rev. A **34**, 7 (1986).

[21] K. Vant, G. Ball, H. Ammann, and N. Christensen, Phys. Rev. E **59**, 2846 (1999).

[22] E. Ott, *Chaos in Dynamical Systems* (Cambridge University Press, Cambridge, England, 1993).

[23] S. Fishman, D. R. Grempel, and R. E. Prange, Phys. Rev. A **36**, 289 (1987).

[24] T. Geisel, G. Radons, and J. Rubner, Phys. Rev. Lett. **57**, 2883 (1986).

[25] N. T. Maitra and E. J. Heller, Phys. Rev. E **61**, 3620 (2000).

[26] R. Ketzmerick, L. Hufnagel, F. Steinbach, and M. Weiss, Phys. Rev. Lett. **85**, 1214 (2000).

[27] C. Mejia-Monasterio, G. Benenti, G. G. Carlo, and G. Casati, Phys. Rev. A **71**, 062324 (2005).

[28] M. V. Berry and M. Robnik, J. Phys. A **17**, 669 (1986).

[29] T. Dittrich and U. Smilanski, in *Quantum Chaos: Between Order and Disorder*, edited by G. Casati and B. Chirikov (Cambridge University Press, Cambridge, England, 1995).